Sensors & Diagnostics

ROYAL SOCIETY OF CHEMISTRY

PAPER

View Article Online
View Journal | View Issue

Check for updates

Cite this: *Sens. Diagn.*, 2025, **4**, 736

Received 27th March 2025,
Accepted 13th June 2025

DOI: 10.1039/d5sd00047e

rsc.li/sensors

Holographic hydrogel bandage sensor for continual monitoring of wound healing†

Yihan Zhang,[a] Yubing Hu,[a] Zhenkang Zhu,[b] Yunuen Montelongo,[c] Yanting Liu,[f] Shihabuddeen Waqar,[a] Yoon Soo Park,[d] Leon CZ Chan,[e] Nan Jiang[fg] and Ali K. Yetisen*[a]

Chronic wounds pose serious health and economic challenges. A low calcium (Ca^{2+}) ion concentration during the early stage often indicates infections. Holographic hydrogel sensors offer label-free sensing platforms, providing real-time and continuous detections of analytes upon diffractive wavelength changes detectable by the naked eye or spectrophotometers, improving the Ca^{2+} ion concentration quantification accessibility. Herein, we present a holographic Ca^{2+} ion bandage sensor using carboxylate-containing hydrogels on polydimethylsiloxane (PDMS) substrates for real-time wound-healing assessment through smartphone readout. Simulations are conducted to investigate the effects of mechanical strength on sensitivity. The holographic Ca^{2+} ion sensor replays blueshifts of 35 nm (hue value change of 7) with 0–4 mmol L^{-1} Ca^{2+} ions, changing colors from dark red to red within 7 minutes. It can accurately and stably (over 24 hours) measure Ca^{2+} ions when bent. The stiffness of PDMS was tuned to balance comfort and sensitivity. In point-of-care settings, holographic bandage sensors, comprising the holographic hydrogel sensor, a backing layer, and a dark cotton layer, can continuously monitor Ca^{2+} ions over 10 hours *via* a smartphone application using hue values. A guiding square in the application assists users in capturing pictures within the inherently narrow viewing angle range of 20–33°. This holographic Ca^{2+} ion bandage sensor facilitates personalized wound assessment through colorimetric interrogation *via* smartphone readout.

1. Introduction

Wound healing is a highly complex biological process affected by numerous factors, such as bacterial colonization, gender, health conditions, and the extent of the injury.[1–3] These factors can prevent normal tissue regeneration and may fail to heal within three months. Globally, 1–2% of the population will experience a chronic wound in their lifetime and impose significant socioeconomic burdens.[4–10] Early intervention and timely treatment can prevent the deterioration of wound conditions and reduce the need for debridement, biological interventions, and amputations. However, conventional wound assessment methods rely on visual inspections and are limited to subjective error and the experience of clinicians. Therefore, a strategy to quantify wound-healing-related biomarkers in the wound milieu is needed. Wound dressings are an ideal biosensor platform due to their mechanical flexibility and ease of operation, which helps reduce patients' pain. The integrated wound dressing sensors should be flexible, breathable, and capable of accurately, timely, and continuously quantifying biomarkers in wound exudates.[11]

Ca^{2+} ions, regulating intracellular signals, are essential electrolytes for cell metabolism and mineral homeostasis.[12,13] Unlike pH level monitoring,[14] which can provide information on the inflammation and infection status, Ca^{2+} ion concentration monitoring can provide more insight into key healing steps, such as fibroblast activities, keratinocyte proliferation, barrier formation, and coagulation at the early stage of the wound-healing process (Fig. 1a).[15] At the point of injury, the concentration increases to 1.84–2.72 mmol L^{-1}, persists during the hemostasis, inflammation, and

---

[a] *Department of Chemical Engineering, Imperial College London, South Kensington, London, SW7 2BU, UK. E-mail: a.yetisen@imperial.ac.uk*
[b] *Department of Chemistry, Imperial College London, South Kensington, London, SW7 2AZ, UK*
[c] *Department of Engineering Science, University of Oxford, Oxford, OX1 3PJ, UK*
[d] *Department of Medicine, Imperial College London, South Kensington, London SW7 2AZ, UK*
[e] *Agency for Science, Technology and Research (A*STAR), Singapore Institute of Manufacturing Technology (SIMTech), 2 Fusionopolis Way, Innovis #08-04, Singapore 138634, Republic of Singapore*
[f] *West China School of Basic Medical Sciences & Forensic Medicine, Sichuan University, Chengdu 610041, China*
[g] *Jinfeng Laboratory, Chongqing 401329, China*

† Electronic supplementary information (ESI) available. See DOI: **https://doi.org/10.1039/d5sd00047e**

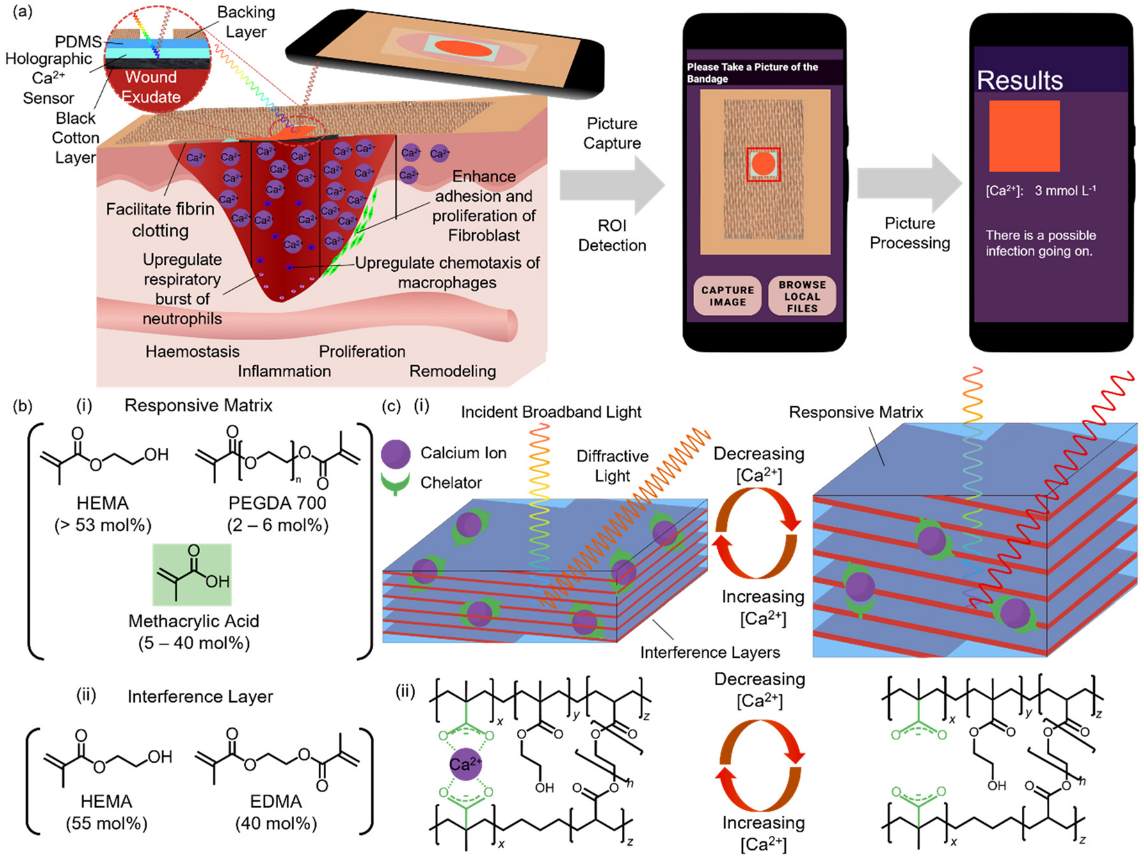

Fig. 1 Real-time detection of Ca^{2+} ion during wound healing using double-photopolymerized holographic sensors. (a) Schematic representation illustrating the role of Ca^{2+} ion levels during different phases of wound healing: hemostasis, inflammation, proliferation, and remodeling. The picture of the bandage taken by the smartphone camera can be processed and analyzed to get the Ca^{2+} ion concentration in the wound milieu and assess the wound healing. (b) Chemical structure of the monomers to synthesize holographic Ca^{2+} ion sensor in i, responsive matrix and ii, interference layers. (c) Working principle of holographic Ca^{2+} ion sensors. i, The shrinkage and swelling of holographic sensors due to the change in Ca^{2+} ion concentration. ii, Mechanism showing the binding of Ca^{2+} ions with MAA, which shrinks the holographic Ca^{2+} ion sensors and causes a blue shift.

proliferation phases, and returns to the normal concentration of 1.2 mmol L^{-1} during the remodeling phase.[13,16] Decreases in the Ca^{2+} ion concentration during the early stages often indicate possible infections and hinder healing, as insufficient concentrations of Ca^{2+} ions may inhibit keratinocyte proliferation, migration toward the wound area, and slow wound healing.[13,17] Wearable Ca^{2+} ion sensing technologies predominantly focus on colorimetric, fluorescence, and electrochemical sensing, but signal drifting and the need for power sources are significant issues for electrochemical sensors, photobleaching and signal interference might affect the accuracy of fluorescence sensors, and the irreversibility of colorimetric sensors also limits broader applications (Table S1†). The need to develop a stable and power-free wearable sensor for accurate, continuous, and real-time wound Ca^{2+} ions monitoring is unmet.

Holographic hydrogel sensors offer a label-free and low-cost optical sensing approach, providing high sensitivity, direct visualization, and long-term stability. They are widely applied for continuous biomarker monitoring.[18–20] Periodic variations of the refractive index (RI) inside holographic sensors are achieved by grating structures of nanocomposites,[21–23] nanoparticles,[24–26] or secondary polymer layers.[18,27] Recently, double-photopolymerization provided a biocompatible nanoparticle-free method to fabricate pH[19] and glucose[18] sensors by creating alternating nanoscale layers with different RIs within functionalized hydrogels. Integrating these sensors with flexible substrates is preferred for medical devices due to their disposability and flexibility. However, previous studies demonstrated that the flexibility of substrates has a significant impact on the sensitivity of holographic sensors.[14,28] This is a tradeoff where the need for conformability must be compromised to maintain the sensitivity, while ensuring it is soft enough to be worn. PDMS has been widely applied in biomedical and biosensing fields as a substrate due to its good mechanical properties, stability, ease of fabrication, oxygen permeability, and optical properties. The tuning of mechanical properties can be done by adjusting the ratio between the elastomer and the curing agent. To overcome this drawback, the mechanical properties of holographic sensor substrates must be tuned to meet both sensitivity and conformability requirements.

Smartphone-based sensing systems have been studied, as smartphones can be used to improve the accessibility of sensors. Smartphones can acquire data in various ways, such as Bluetooth,[29,30] near-field communication,[31,32] cellular networks,[33] and cameras.[34,35] The wavelength shift of holographic sensors can give colorimetric responses, which can be detected by complementary metal-oxide semiconductor (CMOS) sensors quantitatively. Additionally, embedded mobile processing units allow biosensing data to be processed and analyzed directly after readout, providing timely diagnosis and alert.[36] As the data processing power is improving, image processing has become a means to process optical biosensing signals, such as surface plasmon resonance[37] and fluorescence.[34,35] In our previous study,[14] the colorimetric responses can be captured by smartphone cameras, as the color change gave a significant hue value change in captured photographs. This provided an opportunity for smartphone readout to be applied to holographic sensors, where colorimetric signals can be captured by smartphone cameras and then processed to automatically give biomarker levels.

In our previous study, we demonstrated a conformable holographic pH-sensing bandage sensor using a poly(2-hydroxyethyl methacrylate-*co*-ethylene glycol dimethacrylate-*co*-dimethylaminoethyl acrylate) hydrogel on a polyurethane substrate.[14] Based on this foundation, we developed a holographic hydrogel bandage sensor that reversibly and continuously quantifies Ca^{2+} ion concentrations in wound exudates during inflammatory and proliferation phases to provide more clinical insights into the wound-healing process. In this project, the sensor was developed by i) replacing the pH-sensitive functional monomer dimethylaminoethyl acrylate with methacrylic acid (MAA) to enable Ca^{2+} ion sensing; ii) studying the effect of adding inhibitors to optimize the diffraction efficiency; iii) testing the impact of substrate mechanical strength on the sensitivity with PDMS; iv) incorporating the smartphone readout application. Computational simulations facilitated the development of holographic Ca^{2+} ion bandage sensors. Integrating holographic Ca^{2+} ion sensors with PDMS allows bandage sensors to be mounted on wound areas. The selectivity of the bandage was tested across the physiological range of pH and interference concentrations in chronic wounds. A smartphone application was developed to support the readout of holographic sensors *via* smartphone cameras, enabling effective wound assessment in point-of-care (POC) settings.

2. Results and discussion

2.1. Design of holographic hydrogel Ca^{2+} ion sensor

The holographic hydrogel Ca^{2+} ion sensor was fabricated using two monomer solutions as the responsive matrix and interference layers (Fig. 1b). The primary monomer solution (P1) contains 2-hydroxyethyl methacrylate (HEMA), 2–6 mol% polyethylene glycol diacrylate (PEGDA 700), 5–40 mol% MAA, and 1 mol% 2-hydroxy-2-methylpropiophenone (HMPP) (Fig. 1bi). The secondary monomer solution contains 55 mol% HEMA, 40 mol% ethylene glycol dimethacrylate (EGDMA), and 5 mol% HMPP (Fig. 1bii). The responsive matrix was fabricated on a silanized glass slide using the free-radical polymerization of the primary monomer solution to immobilize MAA in polyHEMA hydrogels, generating a responsive matrix sensitive to varying Ca^{2+} ion levels (Fig. 1c). Given the alkaline nature of chronic wounds, the responsive matrix can deprotonate to form carboxylate-rich hydrogels that could bind with Ca^{2+} ions, resulting in a volumetric response. Diffraction gratings were imprinted within the responsive matrix *via* a single-flash Nd:YAG laser (355 nm, 5 ns, 30 μs delay) exposure, which generated periodic differences in RIs as interference layers, thereby creating holographic Ca^{2+} ion sensors. In basic environments of wounds with pH 7.15–8.50, the responsive matrix swells to the largest extent due to deprotonation.[24,38] Two carboxylate groups can bind with one Ca^{2+} ion, increasing the crosslinking density of the responsive matrix. As the responsive matrix shrinks with increasing Ca^{2+} ion concentration, the distance between interference layers decreases, leading to a blue shift in the diffracted light.

2.2. Computational simulation of flexible holographic sensors readout

Simulations facilitated the design of holographic Ca^{2+} ion sensors by visualizing laser exposure and interference layers at the nanoscale using MATLAB R2021b. A graphic process unit accelerated the large-scale simulation *via* parallel computing. In the holographic recording simulation, a planar wave propagated through the simulated hydrogel and was reflected by a planar mirror at the bottom tilted at 5° to match the actual laser optical setup used in experiments (Fig. 2a). This laser interference generated periodic antinode stripes, triggering diffraction gratings formation with varying RIs (Fig. 2b). Fig. 2ci demonstrates the simulation of the holographic sensor readout process using a scanning light source of wavelengths 300–800 nm. The hologram interrogation was tested under 100–150% swelling ratios, resulting in a Bragg peak shift from 406 nm to 588 nm. (Fig. 2cii and iii). Furthermore, simulations allowing for three-dimensional expansion facilitated the design of flexible holographic sensors (Fig. 2di). Under the same swelling ratio increase of 100–150%, the sensitivity of the flexible holographic sensors decreased by approximately three folds, with the Bragg peak shifting from 419 nm to 480 nm (Fig. 2dii and iii). The simulation results theoretically corroborated the observed decrease in the sensitivity of holographic sensors on flexible substrates.[14,28] Nevertheless, the three-dimensional volumetric change shifted wavelength linearly, confirming the feasibility of flexible holographic sensors for quantifying analytes.

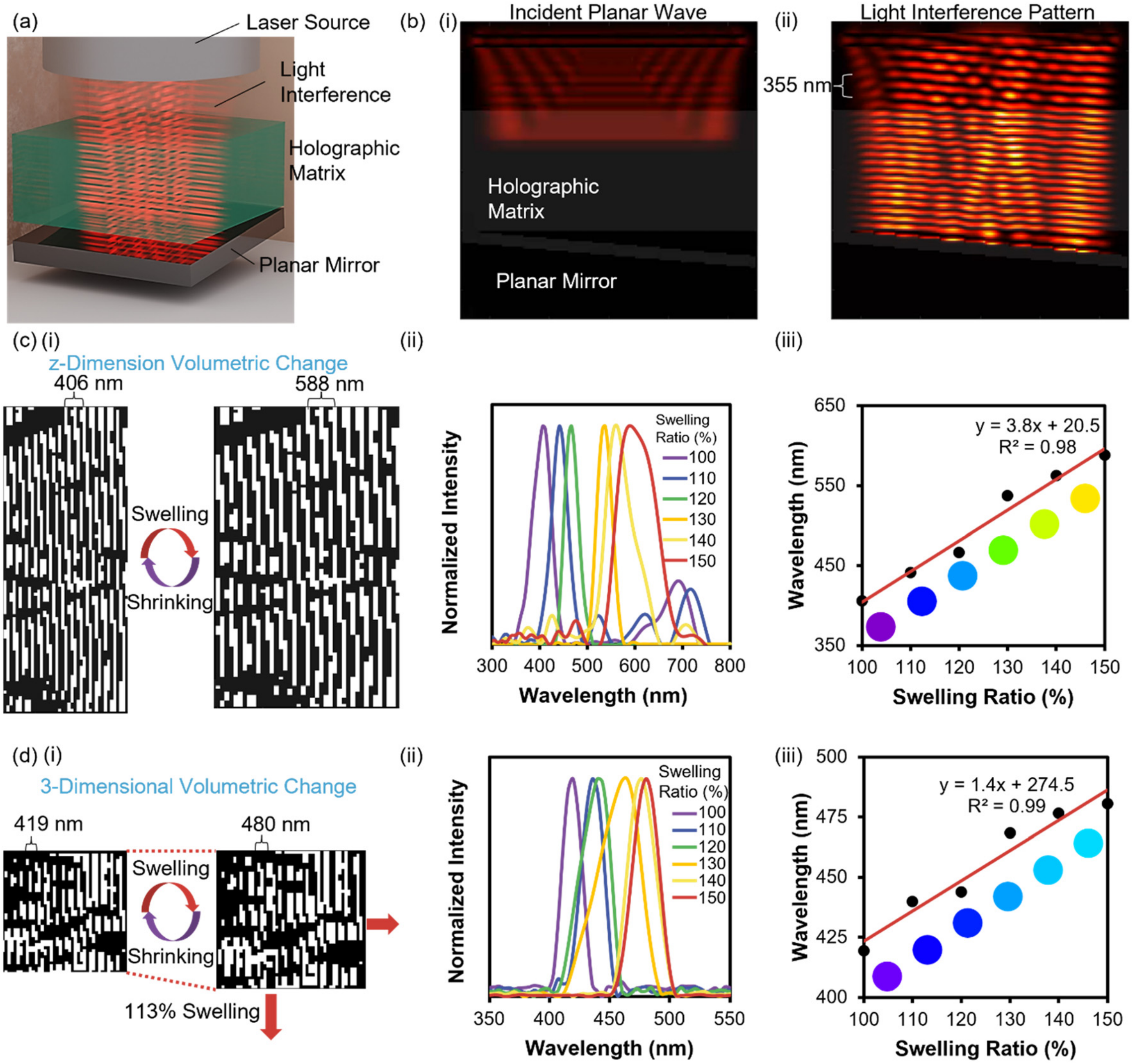

Fig. 2 The three-dimensional simulation of holographic sensors. (a) The schematic represents the three-dimensional simulation of the holographic sensor recording process over a planar mirror at 5° deviated from the holographic matrix. (b) Simulated laser interference during the recording process. (c) The simulation of holographic sensors readout process on rigid substrates that only allows volumetric change on z-dimension. i, Simulated diffraction gratings imprinted in the holographic matrix. ii, Normalized spectra obtained from the simulation at different swelling ratios. iii, Calibration curve obtained from the interrogation simulation of the holographic sensor on the rigid substrate. (d) The simulation of holographic sensors readout process on flexible substrates that allows three-dimensional volumetric change. i, Simulated flexible holographic sensors expanding. ii, Normalized spectra obtained from the simulation at different swelling ratios. iii, Calibration curve obtained from the interrogation simulation of the holographic sensor on the flexible substrate.

2.3. Fabrication of holographic hydrogel Ca^{2+} ion sensors

To maximize the sensitivity to Ca^{2+} ions, holographic sensors were fabricated using 5, 10, 20, 30, and 40 mol% MAA and 2 mol% PEGDA 700. Fig. 3a demonstrates normalized diffractive spectra for holographic sensors with 30 mol% MAA and 2 mol% PEGDA 700 taken by spectrophotometers. The sensitivity increased with the MAA composition in the responsive matrix from 5–30 mol%, and no further increase from a blue shift of 120 nm for 0–4 mmol L^{-1} of Ca^{2+} ions was observed with more than 30 mol% of MAA (Fig. 3b and c). The carboxylic acid group deprotonation in the responsive matrix significantly swelled the hydrogel. The holographic sensors replayed a peak at 880 nm with 0 mmol L^{-1} Ca^{2+} ions and pH 8. The whole physiological range lies within the infrared spectrum, illustrating no distinguishable colorimetric response to the naked eye. 2–6 mol% PEGDA 700 were investigated to alter the replay wavelength range to the visible light. Fig. 3di illustrates the normalized diffractive spectra of the holographic sensors with 30 mol% MAA and 3 mol% of PEGDA 700. Fig. 3dii demonstrated the color change in response to 1.5–3.0 mmol L^{-1} Ca^{2+} ions. The sensitivity reached its maximum at 3 mol% PEGDA 700 and decreased as the composition of PEGDA 700 increased (Fig. 3e and f). The total shift and replay wavelengths remained similar at 85 nm and in the range of 653–750 nm after the PEGDA 700 composition reached 5 mol%.

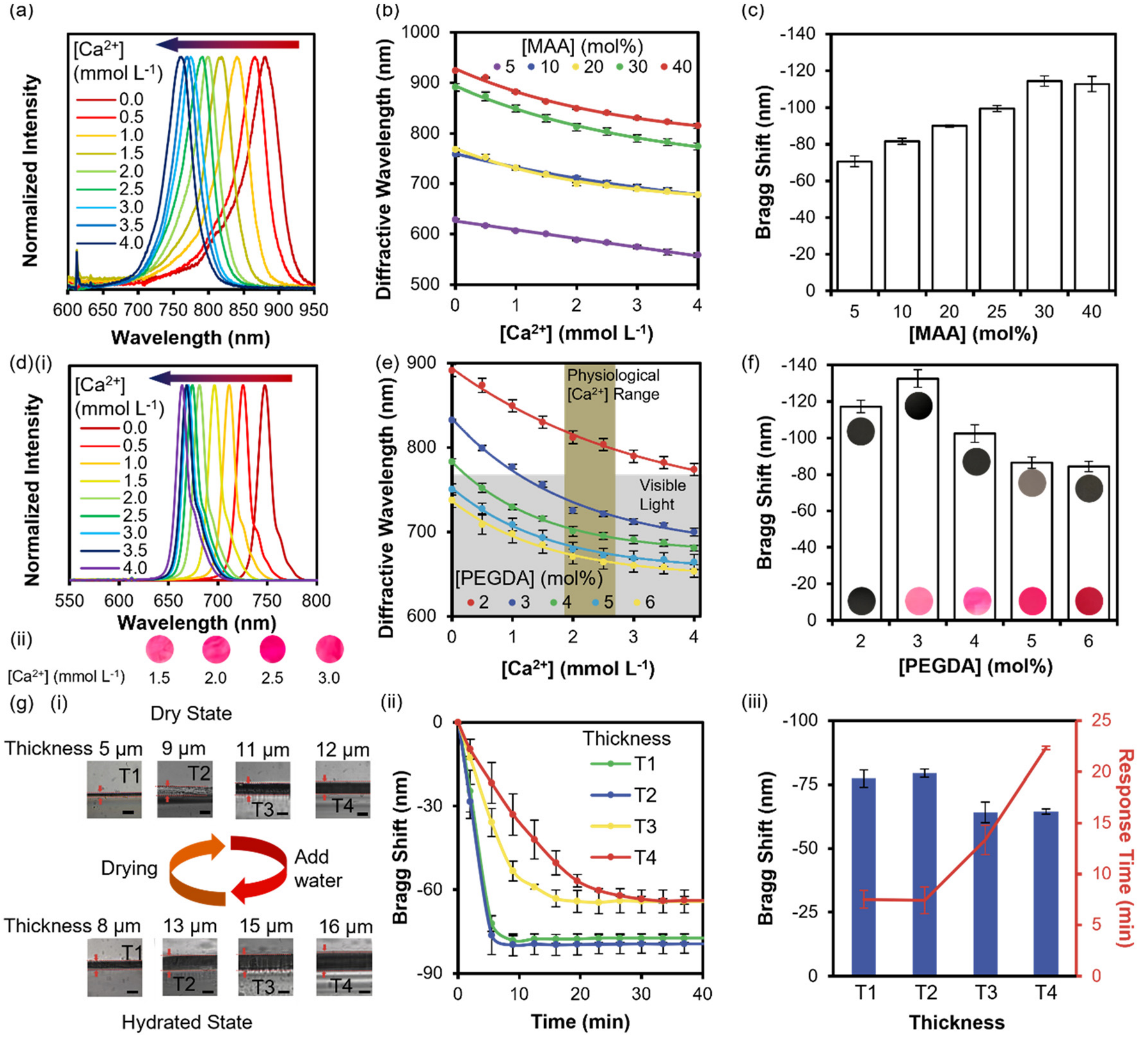

Fig. 3 The physical optimization of the holographic hydrogel Ca^{2+} ion sensor fabrication process. (a) Normalized spectra of holographic Ca^{2+} ion sensors with MAA concentration of 30 mol% and PEGDA 700 concentration of 2 mol%. (b) The effect of MAA compositions on the Bragg peak shift in response to variations in Ca^{2+} ion concentrations in TRIS buffer solution. Error bars represent calculated standard error based on three independent readings (n = 3). (c) The Bragg peak wavelength shift of holographic Ca^{2+} ion sensors with different MAA concentrations (5–40 mol%) on holographic Ca^{2+} ion sensors responding to Ca^{2+} ion concentration of 4 mmol L^{-1}. Error bars represent calculated standard error based on three independent readings (n = 3). (d) i, Normalized spectra of holographic Ca^{2+} ion sensors with 3 mol% PEGDA and 30 mol% MAA. ii, Color pictures of holographic Ca^{2+} ion sensors in TRIS buffer with a Ca^{2+} ion concentration range of 1.5–3.0 mmol L^{-1}. (e) The effect of PEGDA composition on the Bragg peak wavelength in response to variations in Ca^{2+} ion concentrations in TRIS buffer solution. Error bars represent calculated standard error based on four independent readings (n = 4). (f) The Bragg peak wavelength shift of holographic Ca^{2+} ion sensors with 30 mol% MAA and 2–4 mol% PEGDA responding to Ca^{2+} ion concentrations of 0 and 4 mmol L^{-1}. Error bars represent calculated standard error based on four independent readings (n = 4). (g) The effect of the hydrogel thickness on the sensitivity and response time of holographic Ca^{2+} ion sensors. i, Micrographs of holographic Ca^{2+} ion sensors when hydrated with deionized water and dry under the microscope (scale bar = 10 μm). ii, Response time measurement of holographic Ca^{2+} ion sensor for different volumes of P1 solution. Error bars represent calculated standard error based on three independent readings (n = 3). iii, The total shift and response time of holographic Ca^{2+} ion sensors of different thicknesses. Error bars represent calculated standard error based on three independent readings (n = 3).

The thickness of the responsive matrix affects the biomarker diffusion through the hydrogel, influencing the response time and sensitivity of holographic hydrogel sensors.[18] To characterize the impact of hydrogel thickness, the P1 solution with 64 mol% HEMA, 30 mol% MAA, and 5 mol% PEGDA 700 was prepared, and the thickness of the hydrogel was controlled by different P1 solution volumes (20–100 μL). Fig. 3gi demonstrates micrographs of the obtained hydrogels of different thicknesses in dry and swollen states. The Bragg peak shift was taken every 2.5 minutes when the Ca^{2+} ion concentration changed from 0 to 4 mmol L^{-1} (Fig. 3gii). Thicker hydrogels showed decreased sensitivity towards Ca^{2+} ions and a slower response (Fig. 3giii). No significant difference in response time was observed when the P1 volume was less than 50 μL, implying that the binding of Ca^{2+} ions to the carboxylate groups in the responsive matrix became the rate-determining step. The minimum sample volume was tested by pipetting 100, 50, and 25 μL of

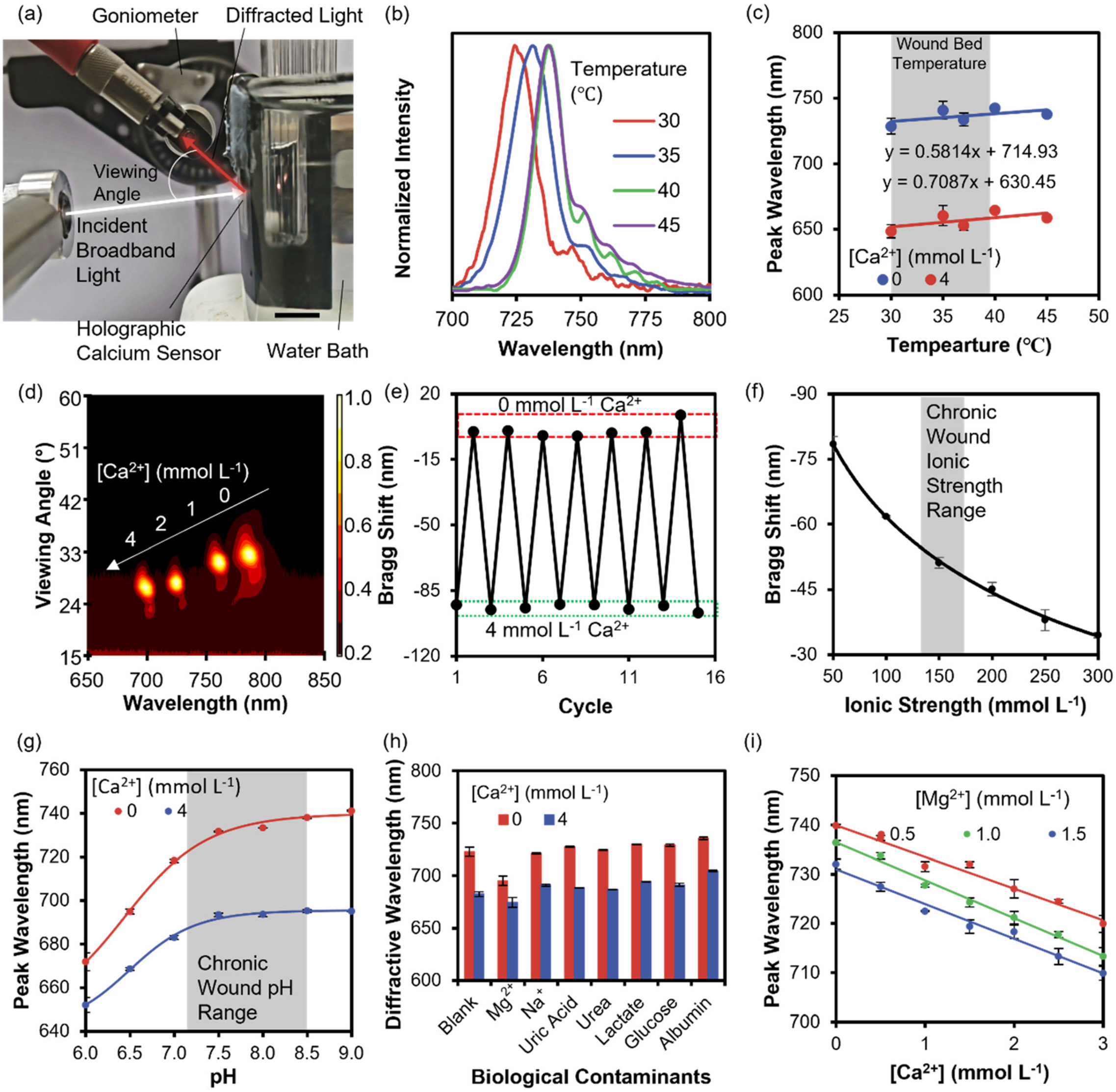

Fig. 4 Characterizations of holographic Ca^{2+} ion sensor. (a) The photo of the holographic sensor interrogation setup at controlled temperature for angle dependence measurements (scale bar = 5 mm). (b) Normalized spectra of holographic Ca^{2+} ion sensors at different temperatures in TRIS buffer solution without Ca^{2+} ions. (c) The diffractive wavelength of holographic Ca^{2+} ion sensors to varying temperatures in TRIS buffer solution with Ca^{2+} ion concentrations of 0 and 4 mmol L^{-1}. The gray-shaded region indicates the temperature range of the wound bed. Error bars represent calculated standard error based on three independent readings ($n = 3$) (d) the angle dependence contour plot of the holographic Ca^{2+} ion sensor at Ca^{2+} ion concentrations of 0–4 mmol L^{-1}, respectively. (e) The reversibility test of holographic Ca^{2+} ion sensor in TRIS buffer solution between Ca^{2+} ion concentrations of 0 and 4 mmol L^{-1}. (f) Ionic strength effect of TRIS buffer solution in the range of 50–250 mmol L^{-1} on the total Bragg shift of holographic Ca^{2+} ion sensors at pH 8. Error bars represent calculated standard error based on three independent readings ($n = 3$). (g) The pH effect of TRIS buffer solution in the range of 6–9 on the total Bragg shift of holographic Ca^{2+} ion sensors. Error bars represent calculated standard error based on three independent readings ($n = 3$). (h) The holographic Ca^{2+} ion sensor was tested in TRIS buffer solution with common interference compounds in TRIS buffer at physiological concentrations (Table S2†). Error bars represent calculated standard error based on three independent readings ($n = 3$). (i) The impact of Mg^{2+} ion level variations of 0.5–1.5 mmol L^{-1} on the holographic Ca^{2+} ion sensor in TRIS buffer solution. Error bars represent calculated standard error based on three independent readings ($n = 3$).

TRIS buffer solution with 0 and 4 mmol L^{-1} Ca^{2+} ion concentrations, respectively (Fig. S1a†). The minimum sample volume was determined to be 50 μL, where there are minimal impacts on the readout (Fig. S1b†).

Since the environment and the healing process can affect the wound bed temperature varying between 30.2–39.5 °C,[39–43] the temperature impacts on holographic Ca^{2+} ion sensors were investigated in a temperature-controlled water bath (Fig. 4a). Fig. 4b and c demonstrate a 12-nm increase in replay wavelengths of holographic Ca^{2+} ion sensors at 30–45 °C, and the holographic sensor only shifted 6 nm at the temperature of 30–40 °C, resulting in negligible differences in the Ca^{2+} ion quantification accuracy within the physiological wound bed temperature. Viewing angle dependence was measured using a rotational stage to vary the angle between the incident light and the receiver fiber optic. The overlay contour plot shows the viewing angle dependence of the holographic Ca^{2+} ion sensor in TRIS buffer with 0, 1, 2, and 4 mmol L^{-1} Ca^{2+} ions, demonstrating good visibility within the range 20–33° (Fig. 4d). The inherently narrow viewing angle range can be overcome by being recorded over a spherical mirror.[14] Fig. 4e demonstrates the reversibility test of the holographic Ca^{2+} ion sensor in the TRIS buffer solution. During 15 cycles of transferring between Ca^{2+} ion concentrations of 0 and 4 mmol L^{-1}, the sensor showed good stability with less than 10 nm difference in the Bragg shift. Moreover, since carboxylic acid groups deprotonation in the responsive matrix can be affected by pH (7.15–8.50) and ionic strength (133–161 mmol L^{-1})[16] in the wound exudates, selectivity tests using TRIS buffer solution with ionic strengths 50–300 mmol L^{-1} and pH 6.0–9.0 were conducted. Higher ionic strength decreased the total blueshift from 80 nm at 50 mmol L^{-1} to only 37 nm at 300 mmol L^{-1} (Fig. 4f). The holographic Ca^{2+} ion sensor also showed a decrease in the total shift and replay wavelengths at a pH lower than 7.5 caused by fewer carboxylate groups (Fig. 4g). Other interferences were added to the TRIS buffer with 150 mmol L^{-1} ionic strength and pH 8. Adding sodium ions, uric acid, urea, lactate, glucose, and albumin only caused a diffractive wavelength difference within 10 nm for both 0 and 4 mmol L^{-1} Ca^{2+} ions since they cannot interact with carboxylate groups in the responsive matrix (Fig. 4h). Mg^{2+} ions are also divalent ions. They exist in a vast amount within the wound milieu (0.75–1.24 mmol L^{-1}) due to the release of Mg^{2+} ions from broken cells. With the presence of 0.94 mmol L^{-1} Mg^{2+} ions, the total blue shift decreased to 21 nm. The binding of Mg^{2+} ions to carboxylate groups shrank the responsive matrix, and therefore, a decrease in replay wavelengths was observed. Since its lower affinity to carboxylate groups, the shrinkage caused by the binding of Mg^{2+} ions was smaller than that of Ca^{2+} ions.[44] To further characterize the impact of Mg^{2+} ion level in the wound milieu on the accuracy of Ca^{2+} ion quantification, the holographic Ca^{2+} ion sensor was tested in TRIS buffer solution at pH 8, 150 mmol L^{-1} ionic strength, 0.5–1.5 mmol L^{-1} Mg^{2+} ions, and 0–3 mmol L^{-1} Ca^{2+} ions (Fig. 4i). The Mg^{2+} ions variation has minimal impact on the sensitivity, but the replay wavelength of the holographic Ca^{2+} ion sensor decreases by approximately 6 nm as the Mg^{2+} ion concentration increases by 0.5 mmol L^{-1}. However, since Mg^{2+} ion concentrations in the wound milieu remain steady, the sensor needs to be recalibrated when Mg^{2+} ions are present. Moreover, the biocompatibility of the materials was tested using cell counting kit-8 (CCK-8) and Live/dead staining assay. The NIH-3T3 was cultured in the responsive matrix extract, the holographic sensor extract, and the Dulbecco's modified Eagle medium (DMEM)-only media, respectively. The biocompatibility of the responsive matrix and holographic sensor was evaluated based on cell growth on days 1, 4, and 7 (Fig. S2).† In the CCK-8 assay, there is no significant difference between the experimental and control groups. The Live/dead staining assay result showed more than 95% cell viability in culture media with the holographic sensor after seven days of culture.

2.4. Characterizations of flexible holographic Ca^{2+} ion sensor

The holographic hydrogel Ca^{2+} ion sensors should be fabricated onto flexible, optically inactive, and non-birefringent substrates to act as wearable analytical devices.[20] PDMS was chosen as substrates due to their excellent biocompatibility and mechanical and optical properties. PDMS is widely used in biomedical applications and as flexible substrates for wearable biosensors, making it an ideal platform to integrate holographic Ca^{2+} ion sensors. Fig. 5a demonstrates the fabrication process of the flexible holographic Ca^{2+} ion sensor. The 160 μm thick PDMS substrates were fabricated by mixing elastomer and the curing agent and cured at 80 °C for an hour. The fabricated PDMS substrates were treated with air plasma and silanized overnight using 3-(trimethoxysilyl) propyl methacrylate in acetone at 1 : 50 (v/v). Meanwhile, a free-standing holographic Ca^{2+} ion sensor was fabricated on an untreated glass slide and then attached to the treated PDMS surface using an adhesive monomer solution of PEGDA 700 and 3 vol% HMPP in DI water at 2 : 1 v/v. The sample was placed under 4 UV(A) strips for 15 minutes and then washed in 50 vol% methanol for 30 minutes to remove unpolymerized monomers. Fig. 5b shows the side view of the flexible holographic Ca^{2+} ion sensor on PDMS substrates before and after use for 24 hours, indicating a reliable bonding between PDMS substrates and sensors. However, since the stretchability of PDMS allows expansions along the substrate, the sensitivity of flexible holographic sensors is lower than those bonded on rigid glass substrates.[14,28] Adjustments in the composition of PDMS were necessary to balance mechanical strength and sensor sensitivity. PDMS substrates with curing-agent-to-base ratios ranging from 1 : 10 to 1 : 2 were tested (Fig. 5c and d). Increasing the curing agent percentage made the PDMS substrates more rigid, restraining the expansion of holographic sensors along the substrate and increasing their total Bragg blue shift from 17 nm to 35 nm. The sensor demonstrated good conformability on curved surfaces with 30–70 mm diameters (Fig. 5e). Bending has minimal impact on flexible holographic sensors at 0–4 mmol L^{-1} Ca^{2+} ions (Fig. 5f). The operation time of flexible holographic Ca^{2+} ion sensors was then tested in buffer solutions with 0, 2, and 4 mmol L^{-1} Ca^{2+} ions, respectively. The flexible holographic sensors demonstrated consistent readout over 24 hours, indicating their reliability in quantifying Ca^{2+} ion levels for wound monitoring at POC settings.

2.5. Smartphone readout of conformable Ca^{2+} ion bandage sensors

The popularity of smartphones has stimulated the development of smartphone-based diagnosis devices due to

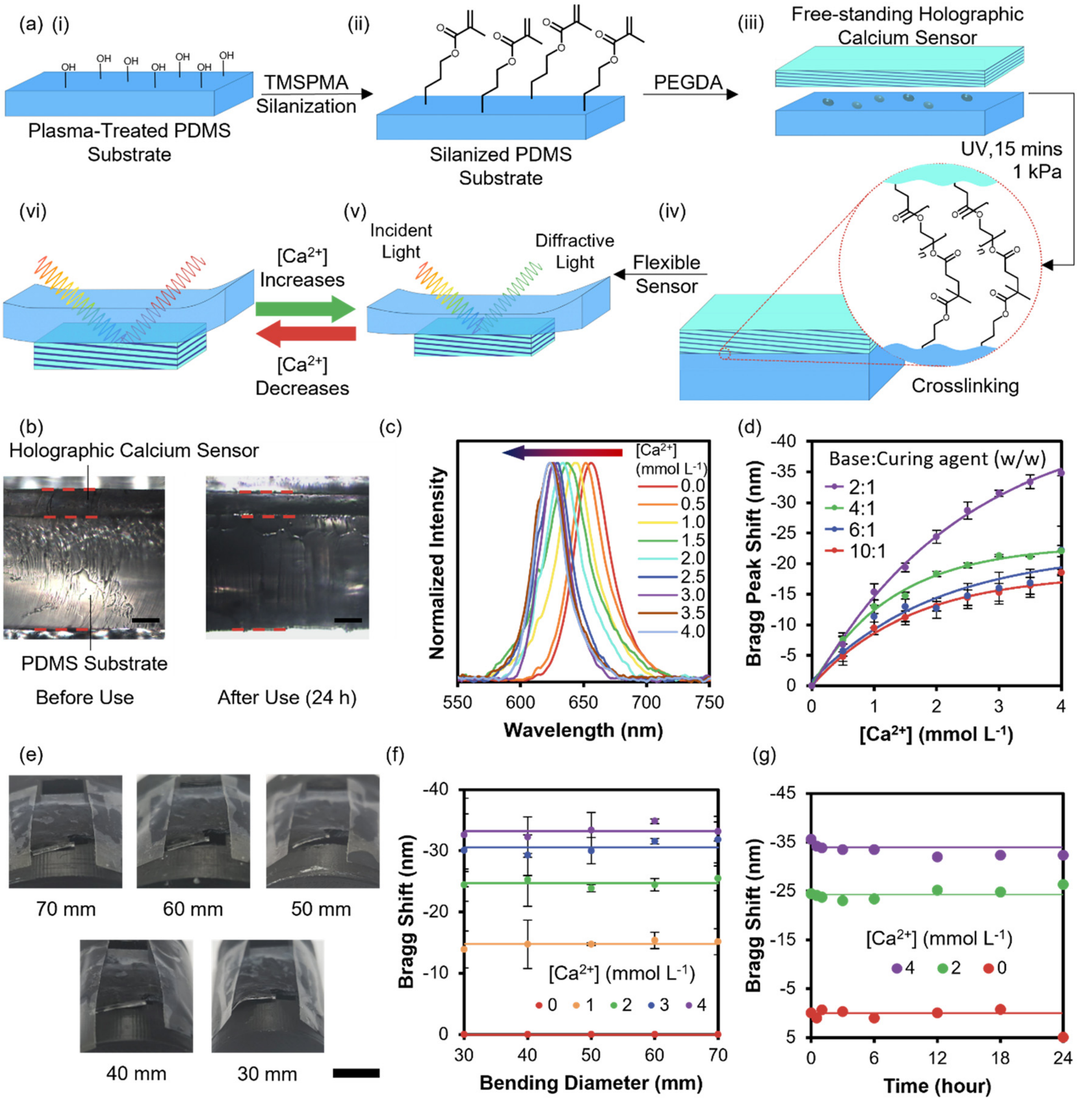

Fig. 5 Fabrication and functionality of flexible holographic Ca^{2+} ion sensors on PDMS substrates. (a) The fabrication process of a flexible holographic Ca^{2+} ion sensor. i, Plasma treatment of PDMS substrates to add hydroxide groups on PDMS surfaces. ii, The silanization of PDMS surface with TMSPMA. iii, Pipette PEGDA 700 solutions on the free-standing holographic Ca^{2+} ion sensor. iv, Sandwich the droplet with the treated PDMS substrate and the free-standing holographic Ca^{2+} ion sensor and place it under the UV light for 15 minutes with a pressure of 1 kPa. v and vi, the working mechanism of flexible holographic Ca^{2+} ion sensors, demonstrating the shrinking and swelling of flexible Ca^{2+} ion sensors at different Ca^{2+} ion concentrations. (b) The side view of the holographic Ca^{2+} ion sensor on PDMS substrates before and after 24 hour usage under the microscope (scale bar = 50 μm). (c) Normalized spectra of holographic Ca^{2+} ion sensors on PDMS substrates of 2 : 1 ratio. (d) The response curve of holographic Ca^{2+} ion sensors on PDMS substrates of different curing agent compositions. Error bars represent calculated standard error based on five independent readings (n = 5). (e) Pictures of bent flexible holographic Ca^{2+} ion sensor on various cylinder surfaces (scale bar = 10 mm). (f) The bending effect on normalized Bragg spectra at Ca^{2+} ion concentration between 0 and 4 mmol L^{-1}, with error bars representing the standard error of four independent readings (n = 4). (g) The operation time of flexible holographic Ca^{2+} ion sensors to 24 hours.

their high accessibility and improved computational power.[36] A dark cotton layer constructed the three-layer sensing bandage, the flexible holographic Ca^{2+} ion sensor, and a breathable cotton-fabric backing layer (Fig. S3†). Dark cotton layers were used to reduce the white scattering from skin surfaces and improve the signal-to-noise ratio. The backing layer can attach the sensor to the skin surface like a plaster (Fig. 6ai). Smartphone cameras can detect the color changes of the bandage sensor (Fig. 6aii). Color information is stored in picture format using HSV, where hue quantifies colors. Fig. 6b demonstrates the smartphone application flowchart for the sensor readout. Pictures can be imported from internal storage or captured *via* camera. The selected picture was white-balanced to remove the impact of different light sources and ambient lighting conditions with the equation below:

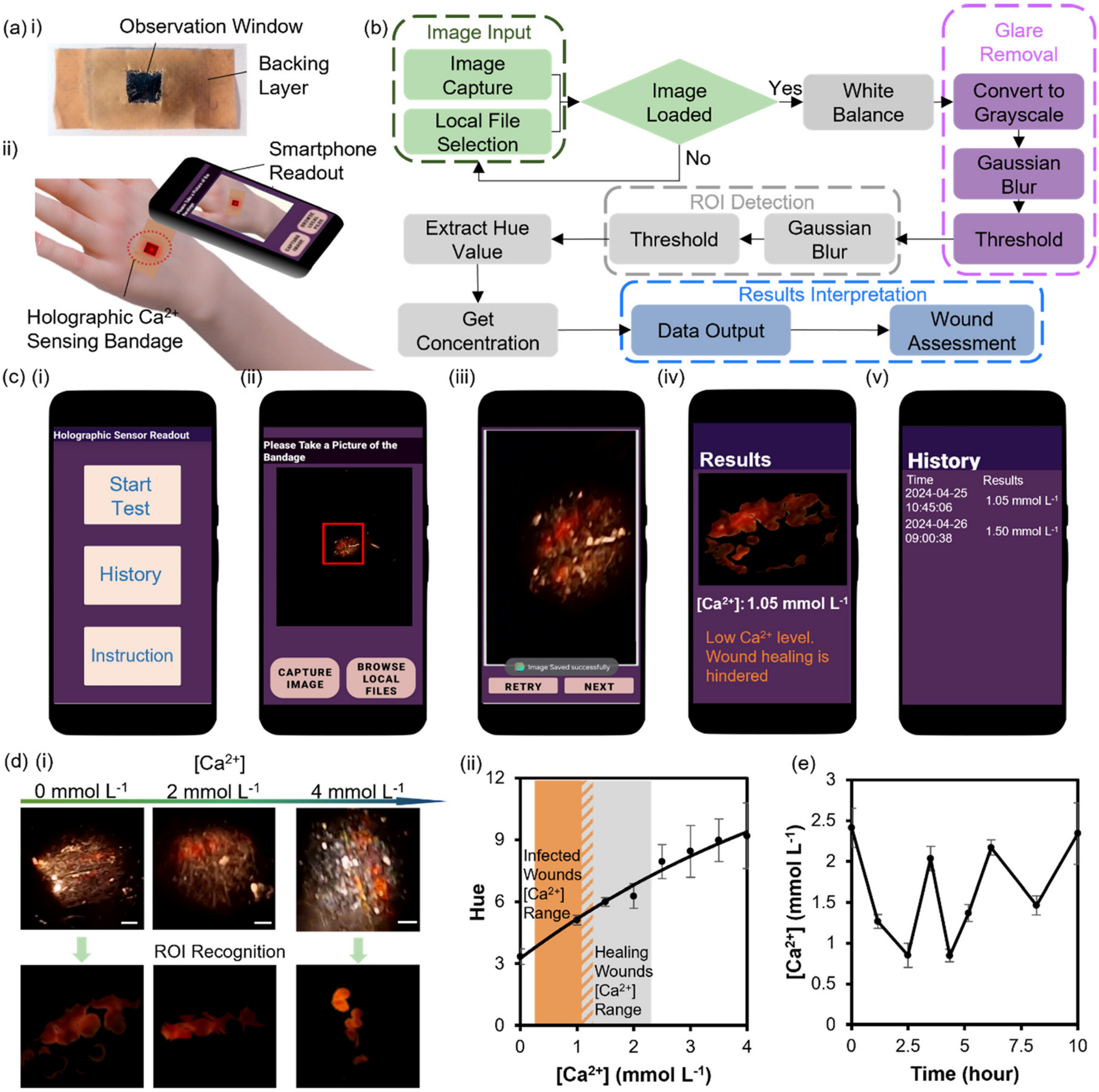

Fig. 6 Smartphone readout of holographic Ca^{2+} ion sensors. (a) The schematic of smartphone readout of holographic Ca^{2+} ion sensors. i, The top view of the holographic Ca^{2+} ion bandage sensor. ii, Schematic of smartphone capturing pictures of the holographic Ca^{2+} ion bandage sensor. (b) The flowchart of the smartphone readout process. (c) The user interface of a developed smartphone application for Ca^{2+} ion concentration quantification, including i, start screen, ii, camera activity for picture taking, iii, loaded picture preview, iv, ROI detection results preview and display of readout result and wound assessment, and v, Display of historical results. (d) The demonstration of smartphone readout of conformable holographic Ca^{2+} ion sensing bandages. i, The demonstration of ROI detection at different Ca^{2+} ion concentrations of 0–4 mmol L^{-1} (scale bar = 1 mm). ii, The average hue value change of detected ROI at Ca^{2+} ion concentrations of 0–4 mmol L^{-1}, where error bars represent eight independent readings (n = 8). The Ca^{2+} ion concentration ranges in infected and healing wounds are illustrated in red and gray shades, respectively.[16,17] (e) Continuous monitoring of Ca^{2+} ion concentration in artificial wound exudate (AWE) simulating an infected wound, where error bars represent three independent readings (n = 3).

$$\begin{cases} a^* = a - \dfrac{1.1(\bar{a}-128)L}{255} \\ b^* = b - \dfrac{1.1(\bar{b}-128)L}{255} \end{cases} \tag{1}$$

where a^* and b^* are corrected a, b values, $\bar{a}$ and $\bar{b}$ are the average a, b values of the original image, and a, b, and L are three channels of CIELAB colorspace. Then, it was processed to remove glares and reflections from the surface of the bandage sensor using Gaussian blur and grayscale thresholding. Pictures without glare can be Gaussian blurred and eroded to denoise the taken pictures. The denoised pictures can then be thresholded to extract the region of interest (ROI) containing the hologram, where the average hue value was extracted and converted to Ca^{2+} ion concentration in wound exudates, providing a quantitative wound assessment.

As shown in Fig. 6ci, on the Start user interface, users can choose to start a new test, view historical results, and read the instructions to facilitate the readout process. To start a new test, the application creates a camera activity allowing users to take pictures of the holographic Ca^{2+} ion bandage sensor or a media selector to load pictures from the internal storage (Fig. 6cii). A red square is provided during the picture-taking to help users locate the sensor from a narrow viewing angle. After loading the picture, the ROI detection algorithm can automatically detect and display the sensing region on the screen (Fig. 6ciii and iv). Once the results are obtained, quantitative wound assessment results are displayed on the analyzed concentration (Fig. 6cv). Results can then be stored in the internal storage and viewed in the future (Fig. 6cvi). Fig. 6di demonstrates that the algorithm can accurately detect the sensing region at 1–4 mmol L^{-1} Ca^{2+} ion concentrations. The smartphone camera readout can be affected by using different camera parameters during the readout. Therefore, camera parameters were fixed during the calibration, (*e.g.* exposure −2.0 using Samsung Galaxy S22). The obtained calibration curve was embedded in the application to automatically convert the extracted hue into Ca^{2+} ion concentrations, allowing for a quantitative assessment of wound healing as the hue value is directly related to human color perception and the dominant wavelength of spectra (Fig. 6dii).[45] The uniformness of grating nanostructure in holographic Ca^{2+} ion sensors ensured diffractive peaks with short full-width at half maximum so that the dominant wavelength can directly interpret the peak wavelength shift and, therefore, the hue value.[46] The sensor was then tested for continuous monitoring *via* smartphone readout of AWE, simulating an infected wound over 10 hours (Fig. 6e). At the point of injury, the calcium level decreased due to bacterial colonization in the wound milieu. The Ca^{2+} ion level remains low in the range of 1–2 mmol L^{-1} until the wound starts to heal after the treatment, where Ca^{2+} ion concentration starts to increase above 2 mmol L^{-1}. Fig. S4† compares the readout results of Ca^{2+} ion concentration from the smartphone readout and the actual Ca^{2+} concentration, demonstrating high consistency between the actual Ca^{2+} ion concentration and the readout results. The results demonstrated good stability and accuracy in monitoring Ca^{2+} ion concentration in AWE over 10 hours, which can provide users with information on the wound healing progression and early diagnosis.

3. Conclusion

In this work, a flexible holographic Ca^{2+} ion bandage sensor was developed on a PDMS substrate supported by a smartphone readout for quantitative wound assessment. The holographic Ca^{2+} ion sensor was fabricated using a double photopolymerization method using carboxylate-rich hydrogels, demonstrating high sensitivity towards Ca^{2+} ions in wound exudates. The sensing system efficiently quantified 0–4 mmol L^{-1} Ca^{2+} ions. The optimized conformable holographic Ca^{2+} ion sensing bandage demonstrated a sensitivity of −8.53 nm $mmol^{-1}$ L in the replay wavelength and a total hue change of 6 in the 0–4 mmol L^{-1} Ca^{2+} ions. The simulation of holographic sensors on rigid and flexible substrates facilitated the fabrication of PDMS substrates to maintain good conformability while constraining the hydrogel from expanding in different directions. Investigating the effect of the mechanical strength of PDMS substrates on sensitivity has provided more insights into the fabrication method of conformable holographic sensors. The conformability of the bandage allows for mounting on body surfaces, providing patients with accurate quantification of Ca^{2+} ions in wound exudates. Integrating smartphone readout further improved accessibility, allowing quantitative wound assessment in POC settings.

However, the integration of flexible substrates decreased the sensitivity of the holographic sensor, resulting in a limited hue value change of 6 when Ca^{2+} ion concentration changes from 0–4 mmol L^{-1}. In addition, the temperature dependence of the sensor might affect the accuracy of readout when the bandage is mounted on the wound surface, since the environment and the healing process can affect the wound bed temperature, varying between 30.2–39.5 °C.[39–43] Moreover, the inherently restricted viewing angle might affect the readout accuracy when taking pictures from different viewing angles. The background color also affects the readout accuracy, as the reflection light from the surface behind the holographic grating can increase the signal-to-noise ratio (SNR).[14] Current mitigations include a dark backing layer and an on-screen alignment guide, with future enhancements such as fixed-angle mounting frames and advanced image-processing algorithms. In this work, we mainly focused on Ca^{2+} ion sensing, while multiplexed sensing (pH and proteases) can be used to get a deeper insight into the wound healing process. Ambient lighting variability also poses a challenge for optical biosensing; our smartphone app already uses white-balance correction during image processing. However, thanks to the advances of machine learning and artificial intelligence algorithms, the impact of ambient lighting conditions can be reduced by using a convolutional neural network.[47] Finally, this study focuses solely on Ca^{2+} ion monitoring. Future efforts will develop multiplexed holographic arrays capable of simultaneous pH, protease, and other biomarker detection to provide a more comprehensive wound-bed profile.

Moreover, the accuracy of wound healing monitoring can be further enhanced by multiplexed monitoring, such as pH, interleukins, and matrix metalloproteinases. By miniaturizing multiple holographic sensors[14] using methods like text patterning,[18] multiplexed holographic bandage sensors can be fabricated to monitor multiple biomarkers simultaneously. Advances in mobile processing units allow efficient processing of high-dimensional biosensing data, provide patients with timely alerts when abnormalities are found, and integrate with artificial intelligence to facilitate personal diagnosis and wound assessment, improving diagnosis accuracy.[36] Moreover, hydrogels have been used for medication delivery to the wound bed during detection.[48,49] The swelling and shrinkage of the hydrogel matrix can control the release of drugs, such as bioactive extracts,[50] anti-inflammatories,[51] and growth factors,[52] offering an opportunity to apply controlled drug delivery with the holographic Ca^{2+} sensor during continual monitoring. The integration of drug delivery to the wound bed during detection enabled on-demand therapy and therefore enhanced wound healing.

4. Experimental section

Materials

All chemicals were analytical grade. PDMS was purchased from Dow and Corning. 3-(trimethoxy silyl)-propyl methacrylate, acetone, hydroxy ethyl methyl methacrylate (HEMA), ethylene glycol dimethacrylate (EGDMA), poly(ethylene glycol) diacrylate (Mn 700; PEGDA 700), methacrylic acid (MAA), 2-hydroxy-2-methylpropiophenone (HMPP), isopropanol, tris(hydroxymethyl)amino methane (TRIS), TRIS hydrochloride (TRIS HCl), potassium chloride, calcium chloride, magnesium chloride, sodium bicarbonate, urea, uric acid, sodium lactate, and hydrochloric acid (1 mol L^{-1}) were purchased from Sigma Aldrich. Methanol, glucose, and sodium chloride were purchased from VWR. Aluminized polyester films were purchased from HiFi Industrial Film Ltd. Cotton layers were purchased from Synergy Health (UK) Ltd. For biocompatibility tests, HEMA and PEGDA 700 were purchased from Shanghai Macklin Biochemical Technology Co., Ltd. (China), HMPP, MAA, methanol, hydroquinone, and isopropanol were obtained from Shanghai Titan Technology Co., Ltd. (China), and EGDMA was purchased from Shanghai Sahn Chemical Technology Co., Ltd. (China). CCK-8, Calcein AM, and propidium iodide (PI) were obtained from APExBIO Technology Co., Ltd. (China). NIH-3T3 fibroblast cells were obtained from the National Collection of Authenticated Cell Cultures (China).

Equipment

Microscope slides were purchased from Fisher Scientific, cover glass slides from VWR and a UVP crosslinker from Analytik Jena. Nd: YAG frequency tripled Quantel Q-smart (5 ns, 355 nm) solid-state laser purchased from Lumibird, France. The drying oven UN30 used for hydrogel drying was purchased from Memmert. The plano-concave lens (−75.0 mm, Ø1″ UV fused silica plano-concave lens, uncoated), optical posts (Ø12.7 mm, *L* = 20 mm), pedestal post holder (*L* = 20 mm, Ø12.7 mm), power and energy meter interface (PM100USB), UV extended Si photodiode, motorized precision rotation stage (Ø1″), collimated laser-diode-dumped DPSS laser module (532 nm, 4.5 mW), laser diode module mounting kit (Ø11 mm), and iris (mounted standard iris, Ø12 mm max aperture, TR3 Post) were purchased from Thorlabs, United States. A 25 mm dielectric 355 nm Nd:YAG laser line mirror was purchased from Edmund Optics, UK. Fisherbrand classic vortex mixer was purchased from Fisher Scientific, Bishop Meadow, UK. The Mettler Toledo FiveEasy Plus™ pH benchtop meter was purchased from Mettler-Toledo Ltd. Orion Star A212 Benchtop Conductivity Meter from ThermoFisher. Holographic responses were analyzed using UV-vis bifurcated fiber optical cables, a 20 W tungsten halogen broadband light source, Flame-S-VIS-NIR-ES spectrophotometer, and Oceanview software (2.0.8) purchased from Ocean Insight. Liquid PDMS was degassed using a vacuum desiccator purchased from Thermo Scientific. PDMS substrate surface treatment was performed using Zepto low-pressure plasma cleaner purchased from Diener Electronic GmbH & Co. KG.

Holographic hydrogel Ca^{2+} ion sensor fabrication

Unless mentioned otherwise, all procedures were carried out in light-tight conditions. Glass slides were silanized using a 3-(trimethoxysilyl) propyl methacrylate in acetone at 1 : 50 (v/v) overnight. The optimized formulation and thickness of the holographic calcium ion sensor were used for fabrication. On the polyester side of a flat aluminized polyester film, 50 μL of the primary monomer solution was pipetted, and a treated glass slide was placed onto the droplet. It was then exposed under 4 UV (A) strip lights for 30 minutes. The polymerized primary hydrogel layer was then removed from the polyester film and washed in methanol and water at a ratio of 1 : 1 (v/v) for 30 minutes to remove any by-products and unpolymerized monomers from the hydrogel layer. The hydrogel was then wiped dry, and 150 μL of the secondary monomer solution was pipetted onto a clean, flat, aluminized polyester film. The hydrogel side was facing downward, and the slide was then placed on the droplet to allow the hydrogel to be soaked in the secondary monomer solution for 10 minutes. The hydrogel surface was then given a single wipe to remove excessive secondary monomer solution. The hydrogel was then dried in an oven at 55 °C for 4.5 minutes. The hydrogel was then left to cool down to 25 °C. Since the thickness of hydrogel at laser exposure is a critical factor affecting replay wavelengths of holographic sensors, these steps must be maintained at the same temperature and humidity. Slides were kept under safe lighting and exposed to a single UV pulse from an Nd: YAG laser (355 nm, 5 ns, 30 μs delay) on the planar mirror with the hydrogel side facing downwards at a tilted angle of 5° from the mirror. While maintaining safe lighting, hydrogels were washed in methanol and DI water (1 : 1 v/v) overnight.

Minimal volume for detection

Place the holographic sensor in a petri dish with the hydrogel side facing upward. 20, 10, 5 μL of sample solution was pipetted onto the sensor area, and then a cover slip was placed on top of the droplet. Between each measurement, the sensor was washed in DI water for 3 minutes and then dried with an air flow.

Biocompatibility test

The culture medium consists of 10% FBS, 1% penicillin–streptomycin solution, and 89% DMEM-HG. The responsive matrix hydrogels and holographic sensors were soaked in culture medium, respectively, for 24 hours to obtain the extract with a concentration of 0.1 g mL^{-1}. 300 NIH-3T3 fibroblasts and 100 μL culture medium were added to each well of the 96-hole plate. After 24 hours, the culture medium was replaced by the responsive matrix extract and the holographic sensor extract, respectively. Live/dead staining and CCK-8 test were used to test cell viability and function at 1, 4, and 7 days.

Live/dead staining

Wash the NIH-3T3 fibroblasts 3 times with PBS buffer to remove dead or damaged cells. Calcein AM and PI were added 1 : 1 to the buffer. After 15 minutes of incubation, the samples were acquired and observed on a fluorescence microscope. Under the microscope, the final signal is observed using blue and green light. By comparing the fluorescence intensities of green fluorescence emitted by calcein AM and red fluorescence emitted by PI, the quantitative relationship between the total number of cells, the number of viable cells and the number of dead cells can be obtained.

CCK-8

The CCK-8 was mixed with the culture medium at 1 : 1000, and 100μL of the mixed solution was added to the 96-well cell culture plate and continued to incubate in the 37 °C incubator for 0.5–1 hours. 450 nm single wavelength detection was performed by an enzyme-labeled instrument.

Free-standing holographic calcium ion sensor fabrication

On the polyester side of a flat aluminized polyester film, 50 μL of the primary monomer solution was pipetted, and a clean, untreated glass slide was placed onto the droplet. It was then exposed under 4 UV (A) strip lights for 30 minutes. The polymerized primary hydrogel layer was then removed from the polyester film and washed in methanol and water at a ratio of 1 : 1 (v/v) for 30 minutes to remove any by-products and unpolymerized monomers from the hydrogel layer. The hydrogel was then wiped dry, and 150 μL of the secondary monomer solution was pipetted onto the hydrogel surface to allow the hydrogel to be soaked in the secondary monomer solution for 10 minutes. The hydrogel surface was then given a single wipe to remove excessive secondary monomer solution. The hydrogel was then dried in an oven at 55 °C for 4.5 minutes. The hydrogel was then left to cool down to 25 °C. Since the thickness of hydrogel at laser exposure is a critical factor affecting replay wavelengths of holographic sensors, these steps must be maintained at the same temperature and humidity. Slides were kept under safe lighting and exposed to a single UV pulse from an Nd:YAG laser (355 nm, 5 ns, 30 μs delay) on the planar mirror with the hydrogel side facing downwards with a tilted angle of 5° from the mirror. While maintaining safe lighting, hydrogels were washed in methanol and DI water (1 : 1 v/v) overnight.

PDMS substrates fabrication

The siloxane was mixed with the curing agent at 2 : 1. The mixture was degassed using a vacuum desiccator, poured into a mold, and covered using clean microscope glass slides to fabricate a PDMS sheet with a thickness of 80 μm. The mold was then placed in an oven at 80 °C for 1 hour. The fabricated PDMS sheet was then removed from the mold, treated using the plasma cleaner, and silanized using a 3-(trimethoxysilyl) propyl methacrylate in acetone at 1 : 50 (v/v) overnight.

Attach free-standing holographic sensor on PDMS substrates

Both free-standing holographic calcium sensors and PDMS substrates were rinsed with methanol to clean surfaces. An adhesive monomer solution was prepared by mixing PEGDA 700 and 3 vol% HMPP in DI water at 2 : 1 v/v. The diluted PEGDA 700 solution was pipetted on the free-standing holographic calcium sensor surface. The PDMS substrate was then placed on the PEGDA 700 solution droplet. A pressure of 1 kPa was applied to facilitate the attachment. The sample was placed under 4 UV (A) strip lights for 15 minutes. The PDMS substrate holographic calcium sensor was carefully removed from glass slides and washed with methanol and DI water (1 : 1 v/v) for 30 minutes.

Selectivity testing

The holographic sensor was tested in TRIS buffer solution containing sodium chloride (128.83 mmol L^{-1}), magnesium chloride (0.94 mmol L^{-1}), calcium chloride (0.00–4.00 mmol L^{-1}), sodium bicarbonate (19.00 mmol L^{-1}), glucose (1.80 mmol L^{-1}), albumin (22 g L^{-1}), potassium chloride (4.40 mmol L^{-1}), urea (8.90 mmol L^{-1}), uric acid (0.35 mmol L^{-1}), and sodium lactate (10.90 mmol L^{-1}), respectively. TRIS and TRIS HCl were added by maintaining TRIS concentration at 50 mmol L^{-1} at a constant pH of 8.00 to stabilize the pH. 3 mmol L^{-1} citric acid was added to stabilize the calcium concentration in AWE. The pH value was corrected using 1 mol L^{-1} hydrochloric acid and confirmed using the pH meter.

Portable spectrophotometer development

The holographic sensors underwent a color change when the calcium ion level changed in the wound milieu. Smartphone-taken pictures can detect these color changes. To improve the accuracy of ROI detection, white balance, glare removal, and denoising (including Gaussian blur and image erosion) were deployed. The ROI detection method was based on the boundary detection algorithm. The ROI was then converted to HSV color space; therefore, hue can be analyzed and corresponded to specific calcium ion concentrations. The calibration curve was embedded in the APP.

Statistical analysis

Spectra taken by the spectrophotometer were firstly processed by the Savitzky–Golay filter and then subtracted by broadband light spectra taken before the measurement. The processed spectra were then normalized to [0,1]. All replay wavelength and Bragg peak shift data were expressed as mean ± standard error. All the above mentioned data processing was carried out using Origin 2020. The overlay contour plots for angle dependence measurements were processed by subtracting previously taken broadband light spectra and then normalized to [0,1]. The data was processed using Python 3.9.7 with Matplotlib and NumPy libraries.

Data availability

The data that support the findings of this study are available from the corresponding author upon reasonable request.

Conflicts of interest

The authors declare no conflicts of interest.

Acknowledgements

A. K. Y. and Y. H. acknowledge the Engineering and Physical Sciences Research Council (EPSRC) (EP/T013567/1). N. J. acknowledges the National Natural Science Foundation of China (82102182), the Fundamental Research Funds for the Central Universities (YJ202152), and JinFeng Laboratory, Chongqing, China (jfkyjf202203001). Y. M. thanks the European Union's Horizon 2020 research and innovation programme under the Marie Sklodowska-Curie grant agreement (896410).

References

1 S. Guo and L. A. Dipietro, *J. Dent. Res.*, 2010, **89**, 219–229.
2 N. X. Landen, D. Li and M. Stahle, *Cell. Mol. Life Sci.*, 2016, **73**, 3861–3885.
3 A. C. Panayi, C. Reitblat and D. P. Orgill, in *Total Scar Management*, Springer Singapore, 2020, ch. 1, pp. 3–16, DOI: 10.1007/978-981-32-9791-3_1.
4 X. Xiao, X. Xiao, A. Nashalian, A. Libanori, Y. Fang, X. Li and J. Chen, *Adv. Healthcare Mater.*, 2021, **10**, e2100975.
5 K. Jarbrink, G. Ni, H. Sonnergren, A. Schmidtchen, C. Pang, R. Bajpai and J. Car, *Syst. Rev.*, 2016, **5**, 152.
6 K. Jarbrink, G. Ni, H. Sonnergren, A. Schmidtchen, C. Pang, R. Bajpai and J. Car, *Syst. Rev.*, 2017, **6**, 15.
7 S. R. Nussbaum, M. J. Carter, C. E. Fife, J. DaVanzo, R. Haught, M. Nusgart and D. Cartwright, *Value Health*, 2018, **21**, 27–32.
8 V. Falanga, R. R. Isseroff, A. M. Soulika, M. Romanelli, D. Margolis, S. Kapp, M. Granick and K. Harding, *Nat. Rev. Dis. Primers*, 2022, **8**, 50.
9 C. K. Sen, *Adv. Wound Care*, 2023, **12**, 657–670.
10 C. K. Sen, G. M. Gordillo, S. Roy, R. Kirsner, L. Lambert, T. K. Hunt, F. Gottrup, G. C. Gurtner and M. T. Longaker, *Wound Repair Regen.*, 2009, **17**, 763–771.
11 A. Pal, D. Goswami, H. E. Cuellar, B. Castro, S. Kuang and R. V. Martinez, *Biosens. Bioelectron.*, 2018, **117**, 696–705.
12 H. Y. Nyein, W. Gao, Z. Shahpar, S. Emaminejad, S. Challa, K. Chen, H. M. Fahad, L. C. Tai, H. Ota, R. W. Davis and A. Javey, *ACS Nano*, 2016, **10**, 7216–7224.
13 T. Subramaniam, M. B. Fauzi, Y. Lokanathan and J. X. Law, *Int. J. Mol. Sci.*, 2021, **22**, 6486.
14 Y. Zhang, Y. Hu, Y. Montelongo, M. Hsu, J. Blyth, N. Jiang and A. K. Yetisen, *Adv. Funct. Mater.*, 2024, **34**, 2308490.
15 P. Salvo, V. Dini, F. Di Francesco and M. Romanelli, *Wound Medicine*, 2015, **8**, 15–18.
16 N. J. Trengove, S. R. Langton and M. C. Stacey, *Wound Repair Regen.*, 1996, **4**, 234–239.
17 Z. Liu, J. Liu, T. Sun, D. Zeng, C. Yang, H. Wang, C. Yang, J. Guo, Q. Wu, H. J. Chen and X. Xie, *ACS Sens.*, 2021, **6**, 3112–3124.
18 S. Davies, Y. Hu, J. Blyth, N. Jiang and A. K. Yetisen, *Adv. Funct. Mater.*, 2023, **33**, 2214197.
19 S. Davies, Y. Hu, N. Jiang, Y. Montelongo, A. Richardson, J. Blyth and A. K. Yetisen, *Biosens. Bioelectron.*, 2022, **207**, 114206.
20 A. K. Yetisen, I. Naydenova, F. da Cruz Vasconcellos, J. Blyth and C. R. Lowe, *Chem. Rev.*, 2014, **114**, 10654–10696.
21 E. Leite, I. Naydenova, S. Mintova, L. Leclercq and V. Toal, *Appl. Opt.*, 2010, **49**, 3652–3660.
22 O. Sakhno, P. Yezhov, V. Hryn, V. Rudenko and T. Smirnova, *Polymers*, 2020, **12**, 480.
23 M. Irfan, S. Martin, M. A. Obeidi, S. Miller, F. Kuster, D. Brabazon and I. Naydenova, *Polymers*, 1858, **2022**, 14.
24 A. J. Marshall, J. Blyth, C. A. Davidson and C. R. Lowe, *Anal. Chem.*, 2003, **75**, 4423–4431.
25 A. G. Mayes, J. Blyth, R. B. Millington and C. R. Lowe, *Anal. Chem.*, 2002, **74**, 3649–3657.
26 S. Kabilan, A. J. Marshall, F. K. Sartain, M. C. Lee, A. Hussain, X. Yang, J. Blyth, N. Karangu, K. James, J. Zeng, D. Smith, A. Domschke and C. R. Lowe, *Biosens. Bioelectron.*, 2005, **20**, 1602–1610.
27 N. Jiang, S. Davies, Y. Jiao, J. Blyth, H. Butt, Y. Montelongo and A. K. Yetisen, *ACS Sens.*, 2021, **6**, 915–924.
28 A. K. Yetisen, H. Butt and S.-H. Yun, *ACS Sens.*, 2016, **1**, 493–497.
29 J. Kim, S. Imani, W. R. de Araujo, J. Warchall, G. Valdes-Ramirez, T. R. Paixao, P. P. Mercier and J. Wang, *Biosens. Bioelectron.*, 2015, **74**, 1061–1068.
30 T. Arakawa, K. Tomoto, H. Nitta, K. Toma, S. Takeuchi, T. Sekita, S. Minakuchi and K. Mitsubayashi, *Anal. Chem.*, 2020, **92**, 12201–12207.
31 G. Xu, C. Cheng, Z. Y. Liu, W. Yuan, X. Z. Wu, Y. L. Lu, S. S. Low, J. L. Liu, L. H. Zhu, D. Z. Ji, S. Li, Z. T. Chen, L. S.

Wang, Q. G. Yang, Z. Cui and Q. J. Liu, *Adv. Mater. Technol.*, 2019, **4**, 1800658.

32 S. G. Kang, M. S. Song, J. W. Kim, J. W. Lee and J. Kim, *Sensors*, 2021, **21**, 703.

33 J. Guo, S. Chen, S. Tian, K. Liu, J. Ni, M. Zhao, Y. Kang, X. Ma and J. Guo, *Biosens. Bioelectron.*, 2021, **181**, 113160.

34 Y. Shi, Y. Zhang, Y. Hu, R. Moreddu, Z. Fan, N. Jiang and A. K. Yetisen, *Sens. Actuators, B*, 2023, **378**, 133128.

35 Y. Wu, Y. H. Zhang, Y. B. Hu, N. Jiang, R. P. Patel, A. K. Yetisen and M. F. Cordeiro, *Adv. Mater. Technol.*, 2024, **9**, 2400238.

36 Y. Zhang, Y. Hu, N. Jiang and A. K. Yetisen, *Biosens. Bioelectron.*, 2023, **219**, 114825.

37 Y. Liu, Q. Liu, S. Chen, F. Cheng, H. Wang and W. Peng, *Sci. Rep.*, 2015, **5**, 12864.

38 B. Greener, A. A. Hughes, N. P. Bannister and J. Douglass, *J. wound care*, 2005, **14**, 59–61.

39 M. Fierheller and R. G. Sibbald, *Adv. Skin Wound Care*, 2010, **23**, 369-379; quiz 380-361.

40 G. Gethin, J. D. Ivory, D. Sezgin, H. Muller, G. O'Connor and A. Vellinga, *Wound Repair Regen.*, 2021, **29**, 843–847.

41 D. Lou, Q. Pang, X. Pei, S. Dong, S. Li, W. Q. Tan and L. Ma, *Biosens. Bioelectron.*, 2020, **162**, 112275.

42 G. Power, Z. Moore and T. O'Connor, *J. wound care*, 2017, **26**, 381–397.

43 Y. Zhang, B. Lin, R. Huang, Z. Lin, Y. Li, J. Li and X. Li, *Microb. Biotechnol.*, 2021, **14**, 1566–1579.

44 D. Wang, A. F. Wallace, J. J. De Yoreo and P. M. Dove, *Proc. Natl. Acad. Sci. U. S. A.*, 2009, **106**, 21511–21516.

45 R. G. Kuehni, *Color Res. Appl.*, 2011, **37**, 424–428.

46 Q. Yao, J. Ju, R. Liang, D. Chen and H. Zhao, *Leukos*, 2013, **10**, 11–18.

47 Z. Wang, Y. Dong, X. Sui, X. Shao, K. Li, H. Zhang, Z. Xu and D. Zhang, *npj Flexible Electron.*, 2024, **8**, 35.

48 N. H. Thang, T. B. Chien and D. X. Cuong, *Gels*, 2023, **9**, 523.

49 R. Marroquin-Garcia, J. Royakkers, M. Gagliardi, R. Arreguin-Campos, T. J. Cleij, K. Eersels, N. M. S. van den Akker, D. G. M. Molin, B. van Grinsven and H. Diliën, *ACS Appl. Polym. Mater.*, 2022, **4**, 2871–2879.

50 A. Kowalczyk, A. Kraskiewicz, M. Weisbrodt and K. Kowalczyk, *Polimery*, 2023, **68**, 461–472.

51 H. T. T. Nguyen, N. H. N. Do, H. D. Lac, P. L. N. Nguyen and P. K. Le, *J. Porous Mater.*, 2022, **30**, 655–670.

52 B. H. Shan and F. G. Wu, *Adv. Mater.*, 2024, **36**, e2210707.